

**VHF Radiation Beam Pattern of Lightning Return Strokes Inferred From
the FORTE Satellite Observations**

Xuan-Min Shao, Abram R. Jacobson, and T. Joseph Fitzgerald

Space and Atmospheric Sciences group,

Los Alamos National Laboratory

Los Alamos, NM 87545, USA

To be submitted to JGR-Atmosphere

LA-UR-03-4013

Abstract

Return-stroke current pulses can propagate at speeds approaching the speed of light c . Such a fast-moving pulse is expected to radiate differently than conventional RF emitters. In this report, we first reexamine the theoretical analysis for the high-speed effect on the radiation beam pattern. Instead of starting with an assumed channel geometry, or with a specific current propagating model, as has been done before by other investigators, we start the analysis with an arbitrarily moving current element. Through a simple differential transformation between the retarded time and stationary time/space, the $(1 - v \cos \theta / c)^{-1}$ factor can be readily obtained. This factor is found to be explicitly associated with radiation beam pattern. We then study FORTE very high frequency (VHF) observations of lightning discharges that were simultaneously detected by the National Lightning Detection Network (NLDN). For these coincident events, the viewing angle from the satellite to the discharges can be derived. During two summers (1998 and 1999) of joint campaigns, 25721 coincidences were found. Among these, 2092 were found to be very narrow (<100 ns), VHF-intense and highly polarized, and were found to be associated with the beginning of return strokes. Through careful statistical analysis regarding the distributions of the event occurrence, we found that the ensemble of all events can be considered to have an isotropic VHF pattern in the upper half space. However, the subset of the return stroke-initiating narrow pulses follows a beam pattern that agrees with a free-space traveling current model at a speed of $0.75c$. We infer that the source for the narrow pulse is associated with the junction point of the attachment process, and the source height is estimated to be a few 10s of meters above the surface of the ground. The physical size of the corresponding discharge is estimated to be less than 22 m.

1. Introduction

Lightning discharges produce radio frequency (RF) radiation over a wide range of the frequency spectrum, from Very Low Frequency (VLF) and below, to Very High Frequency (VHF) and above. At the lower end of the RF spectrum, lightning radiation is believed to be associated with a traveling electric current wave along a well-defined linear channel [Dennis and Pierce, 1964], and the radiation is apparently always polarized. Models that relate the current intensity and movement to the remotely observed radiation field have been developed for return strokes, leader steps, and some general discharge processes, with the main attention focused on the return strokes [e.g., Uman and McLain, 1969, 1970; Uman et al., 1975; Le Vine and Meneghini, 1978a, b; Lin et al., 1980; Runinstein and Uman, 1990; Le Vine and Willett, 1992; Krider, 1992; Thottappillil et al., 1998]. The early works by Uman and colleagues regarding the return stroke showed that the measured radiation field is directly proportional to the propagating current along the channel if the return stroke is assumed to follow a transmission line (TL) model. Using a similar transmission line mode, Uman and McLain [1970] examined the radiation field produced by individual steps of a stepped leader. These early studies were limited to vertically oriented channels and suggested that the radiation field follows a classical dipole beam pattern.

As rightly pointed out by Le Vine and Willett [1992], the previous analyses by Uman and colleagues were not complete, due to the incorrect treatment of the retarded time. Starting from a finite channel segment that sits in the upper space and aligns in an arbitrary direction, Le Vine and Willett [1992] found that the previous inferred dipole field pattern had to be corrected by a factor of $(1 - v \cos \theta / c)^{-1}$, or a “ F ” factor, to accommodate the effect of non-constant retarded time along the channel segment. A dipole pattern is correct only if the speed of the traveling current wave is very small compared to the speed of the light. The analyses of Uman and McLain [1969,

1970] and *Uman et al.* [1975] are valid only under special conditions of that the observer is on the ground and is very distant from the lightning channel, and that the channel under consideration is perfectly vertical, so that θ is constantly 90° along the channel.

Thottappillil et al. [1998] reexamined the effects of the retarded time on the electric field by assuming an extending lightning channel instead of a pre-existent, fixed channel segment as in *Le Vine and Willett* [1992]. Similar radiation pattern in terms of the F factor was derived if the transmission line discharge model was used. For another return stroke model, namely, the “traveling current source (TCS) model” [Heidler, 1986], *Thottappillil et al.* [1998] found a correction factor of $(1 + \cos \theta)^{-1}$ for the radiation pattern. This is not inconsistent with the F factor for the transmission line model, since the TCS model assumes the discharging current travels downward at the speed of light c from the upward-propagating return stroke wavefront.

In both the reports, the analyses started from the integrated contribution along a presumed channel length, with a fixed length by *Le Vine and Willett* [1992] and an extending length by *Thottappillil et al.* [1998]. With the fixed channel segment, the integration is stationary and the F factor arose from the interchange between the spatial and the temporal differentials of the current waveform, assuming a transmission line model and a variable retarded time along the channel. For an extending channel, in addition to the above consideration, the apparent channel length, along which the integration was carried out, was also considered dependent on the retarded time. The physics differences between the fixed and extending channel is that the former assumed that the current was injected into one end of the segment and was terminated or absorbed at the other end, while the latter assumed that the current initiated at the base of the channel and propagated forward without an apparent termination. This difference is the reason for the subtle discrepancy between equation 9a of *Le Vine and Willett* [1992] and equation 38 of *Thottappillil et al.* [1998].

However, if the fixed segment were very long as compared to the scale of the current waveform, solutions from the two reports would become identical. The length of a channel could be considered long if the radiation is due to a very short current pulse (or, equivalently, the radiation is at higher frequencies).

It should be noted that in the field of radio frequency antenna research, a similar problem has been studied regarding the radiation property for a traveling current wave along a wire antenna (see a review by *Smith* [2000]). The analytic result in the time-domain is exactly the same as that reported by *Le Vine and Willett* [1992], except that for the antenna $v \equiv c$, and the corresponding F factor becomes $(1 - \cos \theta)^{-1}$. An antenna has a fixed length, the same as a fixed lightning channel segment as that assumed by *Le Vine and Willett* [1992].

At the high end of the spectrum, i.e., at the VHF and beyond, the radiation is believed to be associated with lightning breakdown processes. At these frequencies, the radiation associated with the common lightning processes like dart and stepped leaders, K-type events, and return strokes is usually unpolarized, indicating that the discharge is an ensemble of randomly directed, incoherent breakdown processes, as reported by *Shao and Jacobson* [2002], based on the FORTE satellite observations. Nevertheless, some temporally isolated, VHF-intense, in-cloud pulses [*Shao and Jacobson*, 2002], as well as a group of very narrow pulses that are associated with the initiation of return strokes [*Jacobson and Shao*, 2002] have been found to be highly linearly polarized. The highly polarized radiation suggests that the radiating current was aligned along a unique, linear path. If the same transmission line model can be used to simulate the discharge process that generates the polarized VHF radiation, one would expect to see the directional effects on the radiation intensity, as suggested by *Le Vine and Willett* [1992] and *Thottappillil et al.* [1998].

In the paper by *Jacobson and Shao* [2002], we reported FORTE satellite observations of very narrow (~ 100 ns), return stroke initiating VHF pulses, and compared them with previous ground-based observations by other researchers. For a detailed review of the ground-based observations, see *Jacobson and Shao* [2002]. It has been found that a small fraction ($\sim 10\%$) of the FORTE-detected return strokes showed such a narrow pulse, and the corresponding strokes were about 4 times more likely to occur over the seawater than over the land. Since these pulses were well polarized and occurred at the beginning of the return strokes, the corresponding discharge is expected to be along a well-defined channel and the channel is expected to be mostly vertical. The vertical orientation is more likely the case when the return stroke occurs over geometrically flat and electrically uniform seawater. On the other hand, the polarized in-cloud VHF discharges obviously do not have a preferred orientation.

Unlike any previous lightning RF observations, all of which had the sensors on or near the ground, the FORTE satellite provides the first opportunity to look at VHF radiation from above. FORTE is in a 70° inclination, 800-km circular orbit, and carries a suite of broadband VHF antennas and receivers. Detailed description of the satellite and its RF and optical payloads can be found in *Jacobson et al.* [1999]. For an individual event that is geolocated, FORTE probes the radiation from a calculable but random viewing angle. If all the events are considered together as a special group, FORTE then views the group from many different possible angles in the upper half space. This situation offers us a unique opportunity of looking into the directional effects of the radiation field due to the fast-traveling current wavefront.

In this paper, we will first revisit the theoretical analysis of the radiation directivity due to a traveling current pulse. Instead of choosing a stationary coordinate frame for the lightning channel and examining the quasi-stationary geometric foreshortening of a finite channel length due to the retarded time, as has been done by previous researchers, we will start with an

infinitesimal moving current element and with a moving frame attached to it. As will be seen, the derivation is more concise and the physical meaning is clearer. We will then examine the FORTE VHF observations for the narrow return-stroke pulses, and will compare the results of the narrow pulses with that of the overall, “background” events. A discussion of the results will be presented.

2. Theoretical Analysis

Figure 1 shows the problem under consideration, in which a current pulse propagates upward along a lightning channel and the radiation field is measured at point $P(x, y, z)$ in the upper half space. The instantaneous vector potential due to the current element (idz') is, in free space,

$$d\vec{A}(t, \vec{r}) = \frac{\mu_0}{4\pi} \frac{i(z', t')}{r(x, y, z, z')} dz' \hat{z}, \quad (1)$$

where

$$t' = t - \frac{r(x, y, z, z')}{c} \quad (2)$$

is the retarded time. Here, dz' is assumed moving along with the current pulse at speed v , rather than stationary in the observer's coordinate frame; z' is the instantaneous position of dz' ; r is the distance from dz' to the observer; and \hat{z} is the unit vector in the motion direction. The direction of \hat{z} is arbitrary and should not be limited to vertical.

As indicated in Equation 2, the retarded time t' is an implicit function of (x, y, z) , in addition to being an explicit function of t , so that any differential operation on (x, y, z) in the stationary frame would need to operate on t' too. This leads to

$$\begin{aligned}
d\vec{B} &= \nabla \times (d\vec{A}) \\
&= \nabla \times (d\vec{A})|_{t'=const} + \nabla t' \times \frac{\partial (d\vec{A})}{\partial t'}
\end{aligned} \tag{3}$$

In the (x, y, z) coordinates, t is uniform so that $\nabla t = 0$, but viewing from stationary P, $\nabla t'$ may not be zero, due to Equation 2. We have

$$\begin{aligned}
\nabla t' &= -\frac{1}{c} \nabla r \\
&= -\frac{1}{c} \nabla r|_{t'=const} - \frac{1}{c} \frac{\partial r(t')}{\partial t'} \nabla t' \\
&= -\frac{\vec{r}}{cr} + \frac{\nabla t'}{c} \frac{(z-z') \frac{\partial z'}{\partial t'}}{\sqrt{x^2 + y^2 + (z-z')^2}} \\
&= -\frac{\vec{r}}{cr} + \frac{\nabla t'}{c} \frac{\vec{v} \bullet \vec{r}}{r}
\end{aligned} \tag{4}$$

Rearranging the above equation, we have

$$\nabla t' = -\frac{\hat{r}}{c(1 - \vec{v} \bullet \vec{r}/c)} \tag{5}$$

The velocity in Equations 4 and 5 is the velocity at time t' . The physical interpretation of Equation 5 is that the retarded time t' is not isotropic in the observer's coordinate frame.

In Equation 3, $d\vec{A} \propto 1/r$ and $\nabla \times (d\vec{A})|_{t'=const} \propto 1/r^2$. For the radiation field, this term can be neglected as compared to the $1/r$ term. Substituting Equation 5 into 3 we have

$$\begin{aligned}
d\vec{B} &= -\frac{\hat{r}}{c(1 - \vec{v} \bullet \vec{r}/c)} \times \frac{\mu_0}{4\pi r} \frac{\partial i(z', t')}{\partial t'} dz' \hat{z} \\
&= \frac{\mu_0}{4\pi c r} \frac{\sin \theta}{(1 - v \cos \theta/c)} \frac{\partial i(z', t')}{\partial t'} dz' \hat{a}_\phi
\end{aligned} \tag{6}$$

Here, θ is the angle between \vec{v} and \vec{r} , and ϕ is the azimuthal angle around the channel. For a plane electromagnetic wave, which is justified for distant observations, we have

$$\begin{aligned}
d\vec{E} &= -c\hat{r} \times d\vec{B} \\
&= \frac{1}{4\pi\epsilon_0 c^2} \frac{1}{r} \frac{\sin\theta}{(1-v\cos\theta/c)} \frac{\partial i(z',t')}{\partial t'} dz' \hat{a}_\theta
\end{aligned} \tag{7}$$

Equation 7 is a rather general result for a traveling current element. No special boundary condition, current model, or channel geometry has been assumed. It shows that the observed radiation amplitude depends on the rate of current change at the source at time t' . The corresponding radiation beam pattern exhibits the F factor $(1-v\cos\theta/c)^{-1}$ in addition to the classical dipole factor of $\sin\theta$. For $v \ll c$, the beam will approximate to a classical dipole pattern. This rather general formula is particularly useful if a short current pulse changes its shape (e.g., current attenuating along typical lightning channels) as it propagates. It should be noticed that in the case of a moving but unchanging current pulse, no far-field radiation will be generated. It should also be noticed that the F factor *always* applies as long as the current element moves.

The previous investigators [e.g., *Thottappillil et al.*, 1998] started the radiation-field evaluations with the conventional term of the time derivative of the current, $\partial i(z',t')/\partial t$, with the time derivative measured in the observer's coordinates. Notice that the current itself is referred to a value at an earlier time t' so the above derivative would represent an apparent measure in the stationary coordinates, which is directionally dependent and can be different than the physical change rate of the current at t' . It was due to this treatment of the current derivative that they came up with radiation formulas that did not explicitly have the F factor (Equations 7 and 8 in *Thottappillil et al.* [1998]). It is not difficult to see that, based on the relation between t' and t in Equation 2 and through a similar derivation as that in Equation 4, $\partial t'/\partial t = (1-v\cos\theta/c)^{-1}$, and the F factor can be readily obtained.

In deriving Equation 6, the induction field term $\nabla \times (d\vec{A})|_{t'=const}$ was ignored due to its faster falloff with distance. It is important to point out though the F factor will not apply to this term. Again, the F factor is caused by the nonlinear *differential* transform between (z', t') and (x, y, z, t) , which occurs only for the radiation term. *Kumar et al.* [1995] claimed that other components of the total electric field (static, induction) should also be “corrected” with a similar F factor; this is clearly wrong.

For an extending discharge like a return stroke, the growth of the channel could be considered as a train coming out of a tunnel. The opening of the tunnel is analogous to the base of the lightning channel, and each section of the train is analogous to the above current element. At time t in the observer’s frame, the length of the extending channel is $L' = vt'$. The total radiation contribution along the channel can be obtained by a line integration of Equation 7. Under special conditions that (1) the channel grows at a constant speed v , (2) the channel is straight, and (3) the channel length is much shorter than the distance between the lightning and the observer ($L' \ll r$), the integration can be carried out as the following

$$\begin{aligned}\bar{E} &= \frac{1}{4\pi c^2 r} \frac{\sin \theta \hat{a}_\theta}{(1 - v \cos \theta / c)} \int_0^{L'} \frac{\partial i(z', t')}{\partial t'} dz' \\ &= \frac{1}{4\pi c^2 r} \frac{v \sin \theta \hat{a}_\theta}{(1 - v \cos \theta / c)} (i(vt', t') - i(0, t'))\end{aligned}\quad (8)$$

If the concept of the transmission line model is used, that is $i(vt', t') = i(0, t' - vt'/v) \equiv i(0, 0)$, and $i(0, 0) = 0$, Equation 8 can be simplified as

$$\bar{E} = -\frac{1}{4\pi c^2 r} \frac{v \sin \theta \hat{a}_\theta}{(1 - v \cos \theta / c)} i(0, t') \quad (9)$$

In addition, if a perfect conducting ground is considered and if the discharge is vertical and right on the surface of the ground, we have

$$\vec{E} = \frac{2}{4\pi\epsilon_0 c^2 r} \frac{v \sin \theta}{(1 - (v \cos \theta / c)^2)} i(0, t') \hat{a}_\theta \quad (10)$$

under the condition of $L' \cos \theta < \lambda/4$. Here, λ is the wavelength at which the radiation is observed. It is clear that at VLF-LF, the wavelength is comparable to or greater than the scale of a typical discharge, and Equation 10, which is derived by adding a time-independent imaginary current source to the original, is valid at most of the times. Lightning radiation has been commonly observed in the VLF-LF range, and a great deal of physical interpretation and understanding of lightning discharges is based on such observations. At VHF, the wavelength is in the range of 1-10 meters; if the source is several meters above the ground, Equation 10 will be invalid. In deriving Equation 10, a transmission line model was assumed. Without this assumption, and for a general upward traveling current element, the term $vi(0, t')$ must be replaced by $\partial i(z', t') / \partial t'$, as that in Equation 7.

Equations 8, 9 are in agreement with the results of *Thottappillil et al.* [1998] regarding a transmission line model. They are also in agreement with *Le Vine and Willett* [1992] if the front end of their channel segment is stretched into positive infinity. Equation 10 agrees with the result reported by *Krider* [1992] in which a perfect conducting ground was used.

Figure 2 shows the relative shapes of the radiation beam patterns for a dipole, a traveling current pulse, both in free space, and a traveling current whose base is on the surface of the ground. The solid curves are for exactly vertical discharges, whereas the dashed curves are for discharges that may not be purely vertical, as will be discussed later. For the on-ground discharge, only the upper half space is meaningful due to the plane, conducting ground. For

sources in free space (the former two cases), any observing angle is possible. The current traveling speed v was assumed to be $0.75c$ for the corresponding models. At this speed, the differences among the three patterns are evident. Nevertheless, as v approaches to zero, all the patterns will become the same dipole pattern.

3. FORTE/NLDN Joint Observations

The FORTE satellite was launched into a 70° inclination, circular orbit at 800 km altitude on August 29, 1997. FORTE carries a pair of linear polarization, log-periodic dipole array antennas (LPA) that have a primary frequency coverage between 30 and 90 MHz. The RF payload includes a pair of independent broadband receivers that each has an analog bandwidth of 22 MHz. Each receiver's output, in the form of electric field E , is digitized at a rate of 50 mega samples per second with a 12-bit resolution. For studies presented in this paper, the receivers (or at least one of the two) were tuned to the range 26-48 MHz. An 8-channel subband trigger system that was designed to overcome the typically overwhelming man-made carrier signals over the analog passband was used to trigger the FORTE data recording system. More detailed and complete descriptions of the FORTE RF payload and their performance have been presented in *Jacobson et al.*, [1999] and *Jacobson and Shao* [2002]. More discussions on the trigger system are to be presented later in this paper.

During the summers of 1998 and 1999, collaborative observations between FORTE and United States National Lightning Detection Network (NLDN) were conducted. NLDN is an array of VLF-LF sensors that covers lightning discharges (mostly cloud-to-ground discharges) throughout the continental United States [*Cummins et al.*, 1998]. The NLDN data were specially postprocessed in a relaxed criterion mode to maximize the detection range for cloud-to-ground (CG) discharges and to include possible in-cloud (IC) discharges. For each detected event, NLDN

provided information on the type of the discharge (e.g., IC, -CG, +CG), the geographic location, and the inferred peak current. During the two summer campaigns, 25721 coincidences were obtained between FORTE's VHF (26-48 MHz) and NLDN's VLF-LF observations. The method for establishing the coincidences, and for characterizing their reliability, was described by *Jacobson et al.*, [2000].

Figure 3 maps all the FORTE/NLDN coincident events (green) over the continental US and the surrounding regions. The red dots indicate the ground strokes that were initiated with a very narrow VHF pulse, as will be further discussed later. A similar plot was presented by *Jacobson and Shao* [2002], in which different types of the discharges were color-coded. Among these, 10763 are -CGs, 5386 are +CGs, 2173 are ICs, and the remaining 7397 are uncharacterized-polarity ground strokes (G). The last category is due to the distant strokes that occurred 625 km or farther from the boundary of the NLDN sensor array. At these distances, due to the ground and ionospheric distortions of the VLF-LF waveform, NLDN was unable to confidently characterize the polarity of the ground strokes nor to evaluate the corresponding peak current. The fractions for different types of discharges mentioned here should not be confused with their natural occurrence. The two monitoring systems are sensitive to two very different portions of the radio spectrum, with NLDN being designed primarily for detection of CGs and FORTE being designed for detection of VHF radiation that can be equally produced by CGs and ICs. The rate of coincidence for a specific event is affected by the different detection biases of the two systems.

For this study, NLDN provided the necessary information in terms of the discharge's geographic location and the general type of discharge (i.e. whether CG and IC for a specific event). Since the position of the FORTE satellite is known for each FORTE detected event, the viewing angle from the satellite to the coincident discharge can be derived, as illustrated in Figure

4. In addition, if the discharge type is labeled as a ground stroke by NLDN, in which case the channel is expected to be more or less vertical, the probing angle referenced to the channel orientation, θ , can be obtained. This provides the necessary foundation for the beam pattern examination.

4. Analysis

4.1. Pulse width examination

Figure 5 shows examples for (a) a “normal” initial –CG stroke, (b) a “normal” subsequent stroke, (c) an initial stroke with a distinct narrow pulse, (d) and a subsequent stroke with a narrow pulse. The type and sequence of the strokes were based on the coincident NLDN observations. For the normal strokes, some commonly observed VHF characteristics are shown. For the initial stroke the radiation is enhanced at the beginning of the return stroke ($\sim 100 \mu\text{s}$ into the record in Figure 5a), and for the subsequent stroke the radiation becomes suddenly quiet after the leader reaches the ground. These properties have been reported from ground-based observations [e.g., Rhodes *et al.* 1994; Shao *et al.*, 1995; Shao *et al.*, 1999] and from the FORTE satellite observations [e.g., Suszcynsky *et al.*, 2000]. The other two strokes, however, consist of a very distinctive, VHF intense and narrow pulse that is coincident with the beginning of the return strokes. Preliminary results regarding this type of stroke were reported in our previous paper [Jacobson and shao, 2002].

In Jacobson and shao [2002], we demonstrated a careful but somewhat tedious method for recovering the true width (“dechirping”) of FORTE recorded pulses. In the frequency range 26-48 MHz, a transionospheric signal will be chirped (i.e., dispersed) significantly by the dispersive ionosphere, such that an impulse on the ground could be stretched into a few 10s of μs

at the satellite, as shown in Figure 5 and in Figure 4a of *Jacobson and shao* [2002]. In the current study, a different, more autonomous “dechirping” method that utilizes a matched-filtering technique is implemented. Through the Earth’s ionosphere, the extra phase delay for a VHF signal can be approximated as [Budden, 1985]

$$\int (d\phi_{free_space} - d\phi_{ionosphere}) = \frac{e^2}{2c\epsilon_0 m_e} \frac{TEC}{f \pm f_c \cos \gamma} \quad (11)$$

Here, TEC is the total electron content integrated along the line of sight; f is the radio frequency (in our case from 26 to 48 MHz); f_c is the electron cyclotron frequency; γ is the angle between the line-of-sight and the Earth’s magnetic field; and \pm represents the “ordinary” and “extraordinary” modes of the transionospheric signal. This equation formulates the phase response of the ionospheric matched-filter. At VHF, the corresponding amplitude response can be assumed unity and frequency-independent.

All the 25721 coincident events were deconvolved with this matched filter to recover the “true” signature of the signals. To do this, we first chose an 8192-point ($\sim 164 \mu s$) section from each FORTE record, with 1/4 of the points ahead of the trigger position and 3/4 of the points following the trigger position. The deconvolution upon this segment was first carried out in the frequency domain according to Equation 11, and the deconvolved data was then transformed back to the time domain. In the time domain, the time-varying power of the signal is computed by summing the squares of the deconvolved data and the Hilbert transform of the deconvolved data. The peak power in this segment was picked out and any point that exceeds $1/e$ of the peak power, or “high point”, is marked. The time width between the first and the last occurrences of the high points were stored to represent the apparent width of the pulse, and the ratio of the peak power to the effective pulse width is used to measure the quality of the pulse. Apparently, for a single,

outstanding pulse in the segment, the ratio would be high, while for a sequence of erratic signals, the ratio would be low. This same process was repeated 80 times over the same data with slight change of TEC values. The initial, raw TEC value was obtained by an incoherent dechirping method, as described by *Jacobson et al.* [1999]. The deconvolution processes would try the TEC values from 80% to 120% of the initial value, at steps of 0.5%. The highest pulse quality among the 80 trials was then selected, and the corresponding peak power and $1/e$ pulse width were recorded as the representative characteristics for the specific FORTE event. Through this process, $f_c \cos \gamma$ was obtained with the International Geomagnetic Reference Field (IGRF) model [Langel, 1992] and was a fixed value for a specific event, and the '+' was used to best match the ordinary ionospheric mode.

Figure 6 demonstrates the deconvolved pulse from the original FORTE pulse shown in Figure 5c. In Figure 6a, the output is shown in a familiar spectrogram format, while in Figure 6b, the time waveform of the power is shown in a much finer, 10 μs interval around the peak. In this case, the $1/e$ pulse width is estimated to be 80 ns.

Figure 7 shows the distribution of the estimated pulse width for all the 25721 events. The minimum pulse width that is physically meaningful should not be less than 40 ns due to the FORTE sampling interval of 20 ns. The maximum width is due to the length of the data segment for the analysis, which was chosen to be $\sim 164 \mu s$. Interestingly, a clear peak can be seen at the widths narrower than 100 ns. These narrow pulses (total of 2092) were also found to be exclusively associated with ground strokes, and are mostly ($> 90\%$) associated with negative strokes. The geolocations of the narrow-pulse strokes are shown in Figure 3 by the red dots. As previously reported by *Jacobson and Shao* [2002], these strokes are more likely to occur over the

seawater than over the land, not only by the total numbers but also by the respective percentages of such strokes over the overall events within each of the two areas.

4.2. Peak E-field, number of events, as function of viewing angle

As illustrated in Figure 4, FORTE viewed each discharge from a certain angle. With thousands of such observations, FORTE effectively viewed the discharges from almost all the possible angles in the upper half space. Specifically, for return strokes, if the channels can be assumed vertical, the ensemble of the FORTE observations would view the channels from all the different elevation angles, necessary for characterizing the beam pattern. It would be ideal if all the return strokes were identical in terms of VHF radiation, as a “standard candle”, so that the associated beam pattern could be measured directly. Unfortunately, this is not the case. Figure 8 shows the peak amplitudes of the FORTE detected radiation after the above-described deconvolution processing, as a function of the zenith angle θ (viewed from the discharge to the satellite, Figure 4). The green dots are for all the coincident events, and the red dots are for the coincident narrow-pulse strokes. It is clear that at any zenith angle, the radiation amplitude can vary over an order of magnitude or greater, for both the overall events and the narrow-pulse events. The wide scattering of the radiation amplitude due to natural lightning makes the direct beam pattern examination difficult, if not impossible. In addition, the general downward trend of the peak amplitude along increasing zenith angle indicates some other (e.g., noise-riding threshold) effects that will also make the direct examination of the beam pattern difficult.

As had been briefly mentioned in *Jacobson and Shao [2002]*, the event distribution of the narrow-pulse strokes, as referring to the viewing angle, is different than that of the overall -CG events. For the current study, we examined this issue a bit further. We split the 90° zenith angle

range into 15 bins as indicated by the dashed lines in Figure 8, with the first bin covering $0-10^\circ$ and the last bin covering $86.1-88.8^\circ$, the bin sizes in between decreasing linearly. The reason for this type of bin selection is to partially accommodate the uneven event distribution (Figure 8) and yet to have a reasonable angular resolution. We accumulated the number of events within each bin and computed the corresponding area on the surface of the Earth associated with each bin. For each bin, the event number was then divided by the surface area, giving the event density normalized to unit area. Figure 9 shows the density distributions for the overall parent events (solid line) and for the narrow-pulse events (dashed line), which were separately normalized to their own maximums. It is clear that the subset of the narrow-pulse strokes displays a significantly different distribution as compared to that of the overall events. In the case of a single radiator and simultaneous all-sky observation, this type of density distribution is statistically equivalent to the detection probability of the same radiator at different zenith angles. Considering that the detection probability must be related monotonically to the radiation intensity, one would suspect that Figure 9 hints the important information regarding different radiation beam patterns for the two different groups of discharges.

4.3. FORTE trigger threshold

To investigate the detection probability shown in Figure 9, the FORTE trigger mechanism needs to be described and examined. FORTE detection of a VHF lightning signal is triggered by a sophisticated 8-channel subband system. Each subband is 1-MHz wide, and the eight subbands are evenly placed in the corresponding 22 MHz radio band. A trigger is generated if 5 out of the 8 subbands detect a signal that is above the pre-commanded threshold, within a certain time interval ($162\ \mu\text{s}$) to accommodate the ionospheric dispersion. The threshold is either set at an absolute

value or at a relative value over a low-pass-filtered noise level. The latter, “noise riding threshold” setup was used during almost all the lightning observations, and the relative level was typically set 14-20 dB (in power) above the background noise level at each subband.

The background noise at each subband was first measured and averaged within a 2 ms interval about each second. The mean of 8 such precedent noise measurements was then registered and updated every second as the current noise level for the specific subband. The noise level, as well as the actual threshold at each subband was recorded in FORTE’s State of Health (SOH) file in the form of E-field amplitude, but were only sampled every 8 seconds. It should be noticed that the clock for the SOH monitoring is not synchronized to the clock of the trigger system. These features introduce some ambiguities and uncertainties between the SOH reported threshold level and the actual level for a specific triggered event, at each subband.

To retrieve an approximate trigger threshold for each lightning event, we extracted from the SOH file the threshold value that is nearest in time to the event. In theory, the time of the extracted threshold could be as far as 4 seconds away from the time the event was triggered. Among the 8 subband thresholds, the mean of the lowest five was estimated, and we use this mean value to represent the possible threshold value for the specific FORTE recorded event. Figure 10 shows the possible thresholds for all the FORTE/NLDN coincident events, in the same format as Figure 8.

It is clear that an accurate threshold level for each specific FORTE lightning event can *not* be obtained, due to the asynchronous SOH sampling and the variable 5-out-of-8 “OR” combination. The inferred threshold is rather an approximation of the actual level that may randomly occur in a certain range. Fortunately, the one-to-one detailed threshold is not absolutely necessary for the beam pattern analysis. As described above, due to the semi-random nature of the lightning radiation intensity itself, the beam pattern will have to be examined by looking into the statistical

properties of the event density distribution, or the detection probability. The threshold itself can be treated as another random parameter in the statistical process, as will be discussed further later.

Figure 10 shows that at any given zenith angle, the inferred threshold can vary in a large range. This is primarily due to the possibility that each event at the same angle could be associated with a different storm that may occur in a different region at a different time under a different satellite pass, so that the associated noise levels (and the threshold) would be independent from each other. As a function of the zenith angle, it is interesting to note that the inferred threshold values display a general downward trend. In an ideal, globally-uniform radio-noise environment, the satellite detected noise background should have been more or less the same no matter where the satellite was. The lightning producing storms should have little effect on the noise level, since (1) the duty cycle of the lightning VHF radiation is very low and (2) on top of that the duty cycle of the noise sampling by FORTE is also very low (2 ms per second). The relative higher threshold/noise at smaller zenith angles must be caused by a noisier background over the continental US and the neighboring regions. As FORTE approaches the boundary of the NLDN coverage (the continental US and surrounding regions, Figure 3) from the outside, the zenith angle from the coincident discharge to the satellite decreases, and at the same time the satellite comes closer to the noisier environment, and therefore the threshold level will increase. The distance d between the satellite and the lightning is directly related to the zenith angle. Nevertheless, the noise sources in general would not collocate with the detected storm, so that there is not a simple $1/d$ relation between the threshold level and the zenith angle. In some cases the satellite may be nearer the noisier sources and the detected lightning may be at the outer boundary, so that the threshold-zenith relation would be reversed. Apparently, the latter cases of outward looking from the satellite failed to compete with the cases of inward looking. This is not surprising, given that the observations span total of 12 months (April-September, 1998, May-

October, 1999), during which the satellite passes would cover the overhead space almost uniformly. With uniform space coverage, the visible area from the satellite to the potential coincident events is bigger than the NLDN coverage by an extra ~ 3000 km (the radius of the instantaneous FORTE field of view) outer boundary. Viewing from a bigger area to a smaller one will increase the probability of looking inward.

The red line in Figure 10 shows the best power-law fit to the threshold values. Transferring the zenith angle to the discharge-satellite distance d , the red line follows a relation like $(d/H)^{-0.42}$, where H is the height of the FORTE orbit, 800 km. This relation will be used later in the beam pattern analysis.

4.4. FORTE antenna pattern

Practically, all antennas have a certain directivity that will respond differently to signals incident from different directions. To study the detection probability as a function of the viewing angle, the directional response (beam pattern) of the FORTE antenna has to be examined.

FORTE's two linear-polarization LPA antennas are mounted orthogonal to each other along the same boom that points to the satellite's nadir direction. One antenna is always aligned to the ram direction of the satellite. As discussed previously by *Shao and Jacobson* [2001], for each antenna, the relative directivity can be approximated by 1 in the H-plane, and by

$$g'(\theta') = \frac{\sin(2\pi\theta' / BW)}{(2\pi\theta' / BW)} \quad (12)$$

in the E-plane, where θ' is the angle between the nadir and the line of sight projection in the E-plane (Figure 4) in the satellite's coordinates, and BW is the beamwidth between the first nulls.

The nadir angle θ' viewing from the satellite can be easily transferred to the zenith angle θ . For the FORTE antenna, BW can be approximated with π .

During the two summer campaigns, FORTE was mostly triggered from the antenna that is orthogonal to the satellite's ram direction. Referenced to the antenna direction, a lightning signal could randomly arrive at any azimuthal direction. To illustrate the azimuthal dependence of the antenna response, Figure 11 shows the distribution of the coincident events around the azimuth. Clearly, it was slightly easier for FORTE to trigger on the events that were at the broadside of the antenna (in front or behind the satellite) than at the endfire (in cross-track). Nevertheless, at any given nadir angle (or zenith angle from the lightning), there is a good mix of events from all the different azimuths, and an averaged antenna response circling the azimuth can be used to represent the antenna response at a certain nadir angle. The averaged response can be expressed as

$$g(\theta) = \frac{1}{\sqrt{2}} \sqrt{1 + [g'(\theta')]^2} \quad (13)$$

Notice that here we implicitly transferred the antenna beam pattern from the satellite coordinates to the lightning coordinates, from nadir angle to zenith angle.

4.5 Probability of FORTE detection of a lightning event

For FORTE to record a lightning event, the event's radiation must exceed the trigger threshold level. To study the probability of an event that meets this condition, the possible radiation amplitude the event may produce, or in other words, the amplitude distribution, needs to be examined. This could be done by looking at the amplitude distribution along a given zenith angle in Figure 8. At the same angle, the discharge-satellite distance is the same for all the

events, and the satellite detected radiation amplitudes reflect the real amplitudes after a common range correction.

To be more thorough on the amplitude distribution, we will “correct” Figure 8 with the $(d/H)^{-0.42}$ threshold relation. The apparent downward trend in Figure 8 is primarily due to the similar trend of the trigger threshold. It should be noticed that the discharge-satellite distance has little effect on the downward trend since whether or not an event triggers FORTE depends on its intensity at the front of the FORTE antenna and the instantaneous trigger threshold but not on where it comes from. The distance is important only if one needs to retrieve the radiation intensity at the source location. Figure 12a shows the “threshold-corrected” amplitudes after correcting each point with a $(d/H)^{-0.42}$ factor, producing a distribution as though the trigger threshold were not dependent on the zenith angle. Based on this new distribution, the amplitude distributions binned at different zenith angles can be directly compared, as shown in Figure 12b. The overall events were grouped into the same 15 bins as in Figure 8. In Figure 12b, the distributions along the 15 bins were normalized by the total numbers of events within each bin, respectively, and are plotted in a linear-log format. The distributions peak at amplitudes near 0.001 v/m. The drop at the left is due to the effect of the trigger threshold. The width of this shoulder is due to the floating threshold level that itself can vary randomly in a certain range, as discussed before (Figure 10). At the right side beyond the threshold, the curves represent the unbiased distributions of the radiation amplitude. It is evident that all the curves have roughly the same linear behavior (in the linear-log plot) at this side.

Based on this analysis, we can infer an exponential amplitude distribution for the lightning produced VHF radiation, as follows

$$\frac{n(x_E)}{N} = \frac{1}{a} e^{-x_E/a} \quad (14)$$

Here, N is the total number of the events, a is the falloff rate of the distribution, x_E is the radiation amplitude, and n is the number of events at x_E .

Equation 14 would be valid if the radiation had an isotropic beam pattern, or if the polarized discharges were probed from a fixed direction. For radiation that is not isotropic, and if the probing direction is not fixed, the distribution can be expressed as

$$\frac{n(x_E, \theta)}{N} = \frac{1}{ab(\theta)} e^{-\frac{x_E}{ab(\theta)}} \quad (15)$$

where $b(\theta)$ represents the beam pattern. Equation 15 can be interpreted with the help of Figure 13. In Figure 13a, three emitters are assumed to sit at the same location and to be vertical. They have identical radiation pattern but have different intensities, and the intensities follow an exponential relation. If one views the emitters along θ_1 an exponential amplitude distribution like that shown in Figure 13b would be obtained (but with only 3 points on the curve). Viewing from another angle θ_2 would yield another exponential curve on which the three corresponding points would shift leftward to smaller amplitudes. The area integrals below the two curves will be the same, equal to the total number of emitters.

Equation 15 can be used as when the observers are all at the same distance from the emitters and the observers are equipped with identical, isotropic VHF antennas. With the FORTE observations, the discharge-satellite distance $d(\theta)$ will change, and the receiving antenna (linear LPA) has its own unique directivity $g(\theta)$. Under these considerations and through similar

arguments as that for Equation 15, the effective amplitude distribution as viewed at the satellite can be written as

$$\frac{n(x_E, \theta)}{N} = \frac{d(\theta) / H}{ab(\theta)g(\theta)} e^{-\frac{x_E d(\theta) / H}{ab(\theta)g(\theta)}} \quad (16)$$

where H is the altitude of the orbit, which represents the shortest discharge-satellite distance, and is used as a reference distance.

Finally, the number of the events that would be detected by the FORTE satellite at each zenith angle depends also on the trigger threshold $X_T(\theta)$, which itself is a function of θ . The event density, or equivalently the detection probability for a single event, can be expressed as

$$\begin{aligned} \frac{\bar{N}(\theta)}{N} &= \int_{X_T(\theta)}^{\infty} \frac{d(\theta) / H}{ab(\theta)g(\theta)} e^{-\frac{x_E d(\theta) / H}{ab(\theta)g(\theta)}} dx_E \\ &= e^{-\frac{X_T(\theta) d(\theta) / H}{ab(\theta)g(\theta)}} \end{aligned} \quad (17)$$

Here, $\bar{N}(\theta)$ is the total number of events above the threshold at the zenith angle θ . Based on the above equation, we see that if $X_T(\theta)$ were zero, we would have $\bar{N}(\theta) / N = 1$, *i.e.*, all the events would be detected at this angle. If $X_T(\theta)$ was zero across the entire zenith range, the detection probability across θ would be uniformly 1.

We now consider further the effects of the trigger threshold on the detection probability. As indicated by Equation 17, it would be ideal if the trigger threshold were a unique function of the zenith angle. Due to the behavior of the trigger system and the nature of the observations (*i.e.*, lightning discharges from different storms, at different times, over different radio noise backgrounds, all contributing to the same zenith angle), the inferred threshold displays a range of uncertainty, as previously shown in Figure 10. Fortunately, this appears to be *not* a problem for

our study. At a given zenith angle, the variations of the threshold for different events closely resemble a random process. Around their mean value, there are likely equal numbers of points below and above. Putting this statistical feature into Equation 17, it is straightforward to find that by using a mean threshold for the lower integration limit would exclude the events that were associated with the lower thresholds, but at the same time it would include extra events that were associated with the higher thresholds. The likely result is that the two factors would compensate each other, and the randomly scattered threshold values would be unaffected, given that there are enough data samples in each angular bin. In the following studies, the best-fit relation $(d/H)^{-0.42}$, the red line in Figure 10, will be used.

So, in Equation 17, the lefthand side represents the event-density distribution, and the righthand side contains the source beam pattern $b(\theta)$ and other parameters. Among these, $X_T(\theta)$ and $g(\theta)$ have just been discussed, H is known (800 km), $d(\theta)$ can be readily obtained through a simple geometric transform, and a is constant depending on the amplitude distribution (Figure 12b).

4.6. Observation and model comparisons

Having discussed all the relevant parameters and established the relation between the beam pattern and the event-density distribution, we are now ready to compare the observed distributions (Figure 9) with the predictions of Equation 17. In Figure 14, the solid line is the observation for all the geolocated events, the same curve as that shown in Figure 9. The dashed line is the simulated result based on Equation 17. For the simulation an isotropic lightning radiation beam pattern, $b(\theta) = 1$ is assumed. Both curves are normalized to their own maximums for comparison. It should be noted here that by examining the detection probability, information

regarding the absolute radiation amplitude is not needed; only the relative shapes of the beam patterns are necessary. In the simulation, we combine all the angular independent constants into a single constant, that include (1) the constant term for the exponential amplitude distribution (Figure 12b), (2) the constant term for the power-law fit of the trigger thresholds, and (3) the $1/\sqrt{2}$ term for the azimuthally averaged FORTE antenna beam pattern. The combined constant was found to be 3.15.

It is clear from Figure 14 that the two curves agree with each other very well, indicating that the beam pattern for the overall ensemble of all geolocated events can be treated as an isotropic pattern. This is not surprising given that the vast majority of the events are unpolarized, or randomly polarized/oriented. In a previous study [*Shao and Jacobson, 2002*] we found that among the 2173 coincident IC events, about 300 were very well polarized. For these IC events, they would not likely to have the same preferred direction and therefore would not contribute to the ensemble beam pattern in any favored direction.

The isotropic beam pattern for the overall distribution can also be inferred from Figure 12b, although not as straightforwardly, in which the radiation amplitude distributions at different angular bins closely agreed with each other. In the analysis related to Equation 15 and Figure 13, we can see that for an isotropic emitter ($b(\theta) = 1$) the amplitude distributions should be the same at all the different zenith angles.

As has been discussed before, for the narrow, linearly polarized pulses that are associated with the beginning of return strokes, the corresponding discharges can be assumed near vertical, due to the adjacent ground plane. In cases that the discharges are not exactly vertical, the effective beam pattern would deviate from the solid lines shown in Figure 2. To examine this effect, we assumed the discharges have an average orientation of vertical, but could still be in any

directions in the upper half space. The possible directions are assumed to follow a Gaussian distribution with a certain standard derivation. Figure 2 compares the beam patterns with derivation from vertical (dashed curves) to that from the pure vertical orientation (solid curves), for the three different models, respectively. The standard derivation from the vertical direction was chosen as 12° . It can be seen that for the dipole pattern, there is not much change. For the traveling current models in the free space and on the ground, the overhead nulls are somewhat filled up. Other than this, there is no significant change in the rest of the beam patterns.

Figure 15 compares the observed event density distribution (solid curve) with the simulations based on the (1) dipole model (dot-dashed curve), (2) free space traveling current model (dashed curve), and (3) on-ground traveling current model (dotted curve), respectively. The simulation processes are the same as that for the isotropic model described above, except that $b(\theta)$ in Equation 17 is replaced respectively with the three different beam models. The speed of the current wave is assumed $0.75c$ for the two traveling current models. Clearly, a dipole radiation model for the narrow pulses could never provide an event density distribution near to what observed. For the on-ground traveling current model, there appear to be some agreement at zenith angles less than 40° but not at greater zenith angles. It is obvious that the free space traveling current model gives the best agreement between the observed and the simulated event-density distributions. The agreement is increasingly better at greater zenith angles, where more observation data points reside (Figures 8, 12a); this makes the agreement between the two even more significant.

We note that to obtain the best fit between the observation and the traveling current models, we tried different traveling speeds for the models (see Equations 7, 9 and 10). We found

that $0.75c$ gives the best results. For the dipole model, the beam pattern is independent of the speed.

Without overcrowding Figure 15, we point out that with the pure vertical models, the simulated event-density distributions are much the same respectively as that presented in the figure, except some slight differences in the zenith angles $0-15^\circ$. This is not unexpected by looking the comparisons in Figure 2.

From Figure 14, we can conclude that the overall parent events as a group show an isotropic radiation beam pattern. This is statistically valid, and is not to say that each individual event among them is an isotropic emitter. For the return stroke-initiating narrow pulses, we can infer that they display a beam pattern that agrees with that of a free space, $v = 0.75c$ traveling current pulse (Figure 15). These conclusions are drawn indirectly from the analysis of the event-density distributions. If the overall parent events are indeed isotropic, the explicit beam pattern for the narrow pulses can be obtained by comparing its event-density distribution to that of the overall events. To do this we first normalize each of the two distribution curves (Figure 9) with the areas under the curves, respectively, such that each is normalized to a total of one event. Such normalized distributions are equivalent to the detection probabilities, as a function of viewing angle. Equation 17 expresses the possible relations between the normalized distribution, the beam pattern, and the other observational parameters. Based on Equation 17 and the fact of that the observational parameters are common to the two distributions, we have, by assuming

$$b_{all}(\theta) = 1,$$

$$\begin{aligned} \frac{\ln(\bar{N}(\theta)/N)|_{all}}{\ln(\bar{N}(\theta)/N)|_{narrow}} &= \frac{\left(-\frac{X_T(\theta)d(\theta)/H}{ab(\theta)g(\theta)} \right)_{all}}{\left(-\frac{X_T(\theta)d(\theta)/H}{ab(\theta)g(\theta)} \right)_{narrow}} \\ &= \frac{b_{narrow}(\theta)}{b_{all}(\theta)} \\ 29 \quad &= b_{narrow}(\theta) \end{aligned} \tag{18}$$

Figure 16 shows the resultant beam pattern for the narrow pulses as being referenced to the overall events. In the figure, we presented the beam pattern in a polar format with the zenith pointing upward and the horizon pointing to the right, the same as Figure 2 but with only one quadrant. The inferred pattern is shown in two different scales (the two solid curves) to compare with the three different theoretic models (Figure 2). The dot-dashed curve is for the dipole model, the dotted curve is for the on-ground traveling current model, and the dashed curve is for the free space traveling current model. Again, it is clear that the inferred beam pattern for the narrow pulse agrees very well with the free space traveling current model, but not with the other two models. The speed of the current wave was assumed $0.75c$.

5. Discussion

From the theoretical analysis of this paper, it is clear that the F factor for the radiation field is an explicit correction over the dipole pattern, as long as a moving current pulse is considered. Apparently, the F factor only applies to the radiation portion of the total field, but not to the static and induction fields. Due to the means of the derivation of Equation 7, it can be seen that the F factor is rather fundamental for a moving current element. *Krider's* [1992] interpretation of the F factor derived by *Le Vine and Willett* [1992] is correct for the radiation term of the total field. Nevertheless, one could start from Equation 7 to obtain specific analytic results for different traveling current models, and the final formula may or may not have an explicit F factor, due to the models themselves.

In this paper, we have analyzed the possible VHF radiation beam patterns for the FORTE/NLDN coincident events. As discussed before, NLDN provided the necessary information on lightning types and geolocations for the FORTE-detected VHF events. Due to the random nature of the radiation intensity associated with the lightning discharges and the “single-

shot” type of FORTE observation for each individual event, there was not a “standard candle” for the reference of the radiation amplitude and there was not a simultaneous all-sky observation. Therefore, the possible beam patterns could not be derived from a simple amplitude-versus-angle analysis. Instead, we investigated the beam patterns from the statistical analysis of the event-density distribution, as a function of the viewing angle between the discharges and the satellite. Since FORTE has a complex trigger system, there was not a simple one-to-one relation between the recorded event and the corresponding trigger threshold. To study the beam pattern, we examined the effects of the variable trigger threshold on the detection of the events. We also took into account the non-isotropic directional response of the FORTE antenna that was used to receive the signals. Based on the observed events themselves, we derived a possible exponential amplitude distribution for the lightning produced VHF signals. Finally, an analytic relation between the FORTE-detected event density and the possible radiation beam pattern was established (Equation 17).

We treated the overall parent events as one group (25721), and extracted the very narrow pulses (<100 ns) that are associated with the initiation of return strokes and are linearly polarized, as another group (2092). It was found that the ensemble of the overall events shows a near isotropic radiation pattern (Figure 14), and the ensemble of the narrow pulses shows a pattern that agrees with a free space traveling current model at the speed of $0.75c$ (Figure 15). Further analysis, comparing the event density distributions between the two groups, shows an explicit beam pattern for the narrow pulses, which again agrees well with the $0.75c$ free space traveling current model (Figure 16).

The inferred speed in this paper appears to be higher than the earlier results ($0.3-0.7c$, *Idone and Orville* [1982]) for average return stroke speed along ~ 1 km channels above the ground. When the observations were taken nearer to the ground, the speed appears to be higher.

For instance, *Wang et al.* [1999] reported speeds of $0.67c$ and $\sim 1c$ for the first 40 m of two triggered-lightning return strokes.

With the pulse width τ and the propagating speed v , we can roughly estimate the physical size of the moving current pulse. If the concept of the transmission line model is used, the length of the current pulse will be $\sim v\tau$. Since the pulses are narrower than 100 ns, the physical size of the corresponding sources will be less than 22 m.

It is not surprising to find the overall events as a group display an isotropic pattern, since the vast majority of the events were unpolarized and are not expected to align along any preferable directions. For the narrow pulses, the orientations of the corresponding discharges were assumed to be nearly vertical, due to the fact that they were associated with the beginning of return strokes, and due to the additional fact of that a large portion of them occurred over flat and uniform seawater (Figure 3). It was pointed out that with a small derivation from the true vertical, the statistical patterns do not change significantly except in the near-zenith direction for the traveling current models (Figure 2). It was interesting to find that the inferred pattern agrees very well with a free-space model but not nearly as well with the on-ground model (Figures 15, 16). This suggests that the source of the narrow VHF radiation was somewhere above the surface of the ground.

As have been discussed before for Equation 10, for a narrow VHF pulse above the ground and an overhead observer, the ground serves as a reflector. The ground-reflected pulse will be delayed in time, and in general will not add to the original pulse either in time or in phase. For instance, if the source of the radiation pulse is 20 m above ground, to an overhead observer, the reflected pulse will arrive 133 ns later, which is entirely separate from the original pulse if its width is 100 ns or less. Figure 17 shows the time delays between the original and the reflected pulses as a function of the zenith angle, for three different source heights (10, 20, and 30 m). For

Equation 10 to work, i.e., to use the ground as a time-independent imager, the height of the source needs to be less than $\lambda/4$ to assure the in-phase addition from the reflection to the original at all the observing angles. At the observing frequencies (26-48 MHz), the wavelengths are in the range 6-11 m, so that the source would have to be within a very few meters above the ground (<10 ns time delay between the original and the reflected pulses), if not right on the ground. On the other hand, for the reflected pulse not to affect the original pulse (to agree with the free-space model), the source needs to be high enough so that the time delay between them would exceed the half-width of the pulse. As shown in Figure 17, for pulse width < 100 ns, a 20-30 m height appears to satisfy the requirement at most of the zenith angles.

One may argue that in the case the source is high enough, the reflected pulse should be separately detected, against the single-pulse phenomenon presented in this paper. This would be the case if the radiation were not highly upward directed, or the source were much higher than 20-30 m. For an upward traveling current pulse, the reflected radiation power could be a very small fraction of the original power, especially at small zenith angles, as shown in Figure 18 for a traveling speed of $0.75c$. It shows that from 0° to 70° , the reflected power is less than $1/e$ of the original power; and the reflected power decreases continuously as the zenith angle decreases. This makes the reflected pulse less visible at most of the viewing angles. Only near to the horizon, the reflected power approaches the level of the original power, but at the same time the temporal separation between the pair decreases (Figure 17), such that it is difficult to distinguish the two pulses sequentially. Therefore, in either case the reflected pulse is less likely to be clearly detected. To see the reflected pulse, the source would have had to be much higher than 20-30 m, i.e., a few 100s of meters; and due to the radiation beam pattern, it could only be seen at zenith angles greater than $\sim 70^\circ$. It should be pointed out that to temporally distinguish the two pulses,

the time delay between them needs to be > 60 ns (3 data points in the 20 ns per point record), which is five times greater than the 10 ns coherence time between the two pulses. Therefore, in the situations (near the horizon) that the two pulses are not temporally distinguishable, they do not necessarily add up in phase to valid Equation 10.

Based on the above discussions, the source height of the narrow pulses is likely to be a few 10s of meters above the surface of the Earth. It is unlikely the sources would be much higher, since (1) these pulses are observed at the very beginning of the return strokes and (2) no distinguishable reflection has been observed. Indeed, these pulses appear to be closely associated with the attachment process of the return strokes. As a stepped leader approaches close to the ground, upward-connecting streamers are emitted from the ground. One of the upward-propagating streamers will connect to the tip of the downward leader, and will start the return stroke process. This junction process is called the attachment process. As reviewed by *Uman* [1987], the junction point has been reported to be 10-50 m above the ground by many different researchers. However, the review was limited to initial strokes. Recently, *Wang et al.* [1999] reported direct observations of the attachment process in two triggered-lightning strokes that were started by dart leaders, similar to the subsequent strokes in nature –CGs. They found that the junction points were several to eleven meters above the tip of a grounded metallic rod, which itself was 4 m tall. Based on lower time resolution streak-camera observations, *Idone* [1990] inferred that the height of the dart-leader/return-stroke junction point in the range 12-27 m. Apparently, the height we inferred in this study agrees well with the heights of the junction point reported by other researchers.

6. Concluding Remarks

Starting from a moving current element and through a simple differential transform between the retarded time and the stationary time/space, the F factor for the radiation pattern can be readily derived. The F factor is a general correction over the classic dipole pattern and applies to the radiation field explicitly.

We studied the FORTE/NLDN coincident events by examining the event density distributions. A model that relates the observed event density to the possible lightning radiation pattern was established, after careful analysis of the relevant parameters. It is found that the overall ensemble of the events shows an isotropic VHF beam pattern. The subset of the narrow pulse events that were associated with the initiation of return strokes shows a pattern that is in good agreement with that of the free-space traveling current model. The propagating speed is found to be $0.75c$, and the height of the radiation sources is inferred to be a few 10s of meters above the surface of the ground. We further estimate the associated physical sizes for the narrow pulses to be 22 m or shorter.

Acknowledgements

We thank Phil Klingner for his help on retrieving the FORTE trigger threshold. This work was performed at the Los Alamos National Laboratory under the auspices of the U.S. Department of Energy.

References

Budden, K.G., *The Propagation of Radio Waves*, Cambridge Univ. Press, New York, 1985.

Cummins, K. L., M. J. Murphy, E. A. Bardo, W. L. Hiscox, R. Pyle, and A. E. Pifer, Combined TOA/MDF technology upgrade of U.S. National Lightning Detection Network, *J. Geophys. Res.*, *103* (D8), 9035-9044, 1998.

Dennis, A.S., and E.T. Pierce, The return stroke of the lightning flash to earth as a source of VLF atmospherics, *J. Res. Natl. Bur. Stand. Sect. D*, *68*, 77-794, 1964.

Heidler, F., Some deductions from the traveling current source model, paper presented at the 6th International Zurich Symposium on Electromagnetic Compatibility, Inst. Of Telecommunications, Wriclaw, Poland, 1986.

Idone, V.P., and R.E. Orville, Lightning return stroke velocities in the Thunderstorm Research International Program (TRIP), *J. Geophys. Res.*, *87*, 4903-4915, 1982.

Idone, V.P., Length bounds for connecting discharges in triggered lightning subsequent strokes, *J. Geophys. Res.*, *95*, 20,409-20416, 1990.

Jacobson, A. R., S. O. Knox, R. Franz, and D. C. Enemark, FORTE observations of lightning radio-frequency signatures: Capabilities and basic results, *Radio Sci.*, *34*, 337-354, 1999.

Jacobson, A. R., K. L. Commins, M. Carter, P. Klingner, D. Roussel-Dupre, and S. O. Knox, FORTE radio-frequency observations of lightning strokes detected by the National Lightning Detection Network, *J. Geophys. Res.*, *105* (D12), 15,653, 2000.

Jacobson, A.R., and X.M. Shao, FORTE satellite observations of very narrow radiofrequency pulse associated with the initiation of negative cloud-to-ground lightning stroke, *J. Geophys. Res.* 107(D22), 4661, doi:1029/2001JD00152, 2002.

Krider, E.P., On the electromagnetic fields, Poynting vectors, and peak power radiated by lightning return strokes, *J. Geophys. Res.* 97(D14), 15,913-15917, 1992.

Kumar, R., J. Rai, and V. Singh, Lightning return stroke electric fields above ground, *J. Atmos. Terr. Phys.*, 57, 1247-1254, 1995.

Langel, R.A., International Geomagnetic Reference Field: The 6th generation, *J. Geomag. Geoelectr.*, 44(9), 679-707, 1992.

Le Vine, D.M., and R. Meneghini, Simulation of radiation from lightning return strokes: The effects of tortuosity, *Radio Sci.*, 13, 801-809, 1978a.

Le Vine, D.M., and R. Meneghini, Electromagnetic fields radiated from a lightning return stroke: Application of an exact solution to Maxwell's equations, *J. Geophys. Res.*, 83, 2377-2384, 1978b.

Le Vine, D.M., and J.C. Willett, Comment on the transmission line model for computing radiation from lightning, *J. Geophys. Res.* 97(D2), 2601-2610, 1992.

Lin, Y.T., M.A. Uman, and R.B. Standler, Lightning return stroke models, *J. Geophys. Res.*, 85, 1571-1583, 1980.

Rhodes, C. T., X. M. Shao, P. R. Krehbiel, R. J. Thomas, and C. O. Hayenga, Observations of lightning phenomena using radio interferometry, *J. Geophys. Res.*, *99*, 13059-13082, 1994.

Rubinstein, M., and M.A. Uman, On the radiation turn-on associated with traveling current discontinuities in lightning, *J. Geophys. Res.*, *95*, 3711-3713, 1990.

Shao, X. M., P. R. Krehbiel, R. J. Thomas, and W. Rison, Radio interferometric observations of cloud-to-ground lightning phenomena in Florida, *J. Geophys. Res.*, *1000* (D2), 2749-2783, 1995.

Shao, X.M., C.T. Rhodes, and D.N. Holden, RF radiation observations of positive cloud-to-ground flashes, *J. Geophys. Res.*, *104* (D8), 9601-9608, 1999.

Shao, X.M., and A.R., Jacobson, Polarization observations of broadband VHF signals by the FORTE satellite, *Radio Sci.*, *36*, 1573-1589, 2001.

Shao, X.M., and A.R., Jacobson, Polarization observations of lightning-produced VHF emissions by the FORTE satellite, *J. Geophys. Res.*, *107* (D20), 4430, doi:10.1029/2001JD001018, 2002.

Smith, G.S., Teaching antenna radiation from a time-domain perspective, *Am. J. Phys.*, *69*(3), 288-300, 2000.

Suszcynsky, D. M., M. W. Kirkland, A. R. Jacobson, R. C. Franz, S. O. Knox, J. L. L. Guillen, and J. L. Green, FORTE observations of simultaneous VHF and optical emissions from lightning: basic phenomenology, *J. Geophys. Res.*, *105* (D2), 2191-2201, 2000.

Thottappillil, R., M.A. Uman, and V.R. Rakov, Treatment of retardation effects in calculating the radiated electromagnetic fields from the lightning discharge, *J. Geophys. Res.* 103(D8), 9003-9013, 1998.

Uman, M.A., and D.K. McLain, Magnetic field of lightning return strokes, *J. Geophys. Res.*, 74, 6899-6910, 1969.

Uman, M.A., and D.K. McLain, Radiation field and current of the lightning stepped leader, *J. Geophys. Res.*, 75, 1058-1066, 1970.

Uman, M.A., D.K. McLain, and E.P. Krider, The electromagnetic radiation from a finite antenna, *Am. J. Phys.*, 43, 33-38, 1975.

Uman, M.A., *The Lightning Discharge*, Academic Press, Inc., New York, 1987.

Wang, D., V.A. Rakov, M.A. Uman, N. Takagi, T. Watanabe, D.E. Crawford, K.J. Rambo, G.H. Schnetzer, R.J. Fisher, and Z.-I. Kawasaki, Attachment process in rocket-triggered lightning strokes, *J. Geophys. Res.*, 104 (D2), 2143-3150, 1999.

Figure Captions

Figure 1. Geometry of the traveling current element and the observer.

Figure 2. Theoretic beam patterns of radiation E -field for (1) free space dipole ($\sin \theta$), (2) free space traveling current ($\sin \theta / [1 - v \cos \theta / c]$), and (3) on-ground traveling current ($2 \sin \theta / [1 - (v \cos \theta / c)^2]$). Solid curves are for purely vertical channels; dashed curves are for channels that are expected to be vertical but may statistically deviate from the vertical by a certain extent ($\sigma(\theta) = 12^\circ$). The speed v for the traveling current is assumed $0.75c$.

Figure 3. Geographic locations of FORTE/NLDN coincident events. Green dots for the overall events; red dots for the very narrow, return stroke-initiating events.

Figure 4. Geometry of the terrestrial lightning and the FORTE satellite.

Figure 5. FORTE VHF observations of (a) a “normal” initial stroke, (b) a “normal” subsequent stroke, (c) an initial stroke started with a narrow pulse, and (d) a subsequent stroke started with a narrow pulse.

Figure 6. (a) Pulse in Figure 5c after matched filtering deconvolution process. (b) Fine time waveforms of the radiation power around the pulse.

Figure 7. Pulse width ($1/e$ of peak power) distribution for all the coincident events. Pulses that are narrower than 100 ns are considered as narrow pulses in this study.

Figure 8. Peak radiation amplitudes (E) for all the coincident events (green) and the narrow pulses (red), as functions of the zenith angle (Figure 4).

Figure 9. Distributions of area-normalized number of events (event density), at the angular bins shown in Figure 8. Solid curve is for the overall events and dashed curve is for the narrow pulses. Each curve is normalized to its maximum for comparison.

Figure 10. Apparent FORTE trigger threshold for all the coincident events. Red line indicates the best power-law fit to the scattered points, $1.31 \times 10^{-4} (d/H)^{-0.42}$.

Figure 11. Event distribution around the azimuth as being viewed from the satellite. Slightly more events were triggered in the ram direction than in the cross-track direction due to the antenna directivity.

Figure 12. (a) “Threshold-corrected” peak E -fields for all the events. (b) E -field amplitude distributions at the 15 angular bins.

Figure 13. Relations between (a) the radiation beam pattern and (b) the angularly-dependent amplitude distributions.

Figure 14. Comparing the event density distributions between the overall events (solid) and the model simulation (dashed, Equation 17). An isotropic model $b(\theta) = 1$ is used for the simulation.

Figure 15. Comparing the event density distributions between the narrow pulses (solid) and the model simulations of a dipole (dot-dashed), an on-ground traveling current (dotted), and a free space traveling current (dashed). A statistical direction deviation of $\sigma(\theta) = 12^\circ$ from vertical ($\bar{\theta} = 0$) is used for the simulations. The speed v is assumed $0.75c$ for the two latter models

Figure 16. Direct beam pattern comparisons between that of the narrow pulses and the three different models. The former is inferred by comparing the event density distributions between the narrow pulses and the overall events, according to Equation 18. The models are the same as that presented in Figure 2.

Figure 17. Time delay between the original and the reflected pulse at the satellite. For source 30 m above ground, the delay is greater than 50 ns at most of the zenith angles.

Figure 18. Power ratio of the reflection to the original, for $v = 0.75c$ free space traveling current radiation. At zenith angles less than 70° , the ratio is smaller than 0.5. Only near the horizon, powers between the two are comparable.

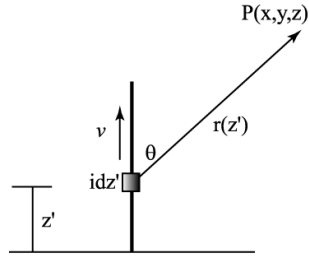


Figure 1

Figure 1. Geometry of the traveling current element and the observer.

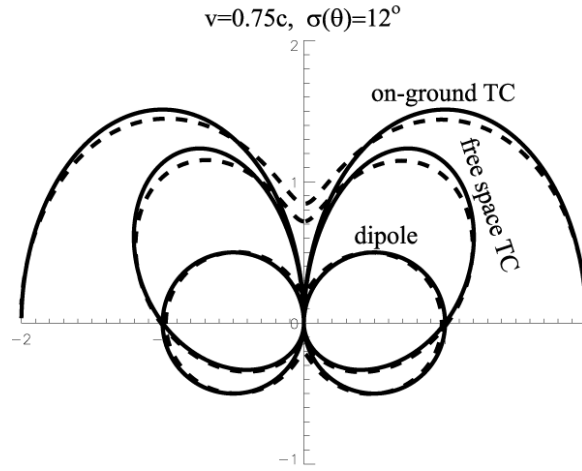


Figure 2

Figure 2. Theoretic beam patterns of radiation E -field for (1) free space dipole ($\sin \theta$), (2) free space traveling current ($\sin \theta / [1 - v \cos \theta / c]$), and (3) on-ground traveling current ($2 \sin \theta / [1 - (v \cos \theta / c)^2]$). Solid curves are for purely vertical channels; dashed curves are for channels that are expected to be vertical but may statistically deviate from the vertical by a certain extent ($\sigma(\theta) = 12^\circ$). The speed v for the traveling current is assumed $0.75c$.

Green: overall events; Red: narrow pulse events

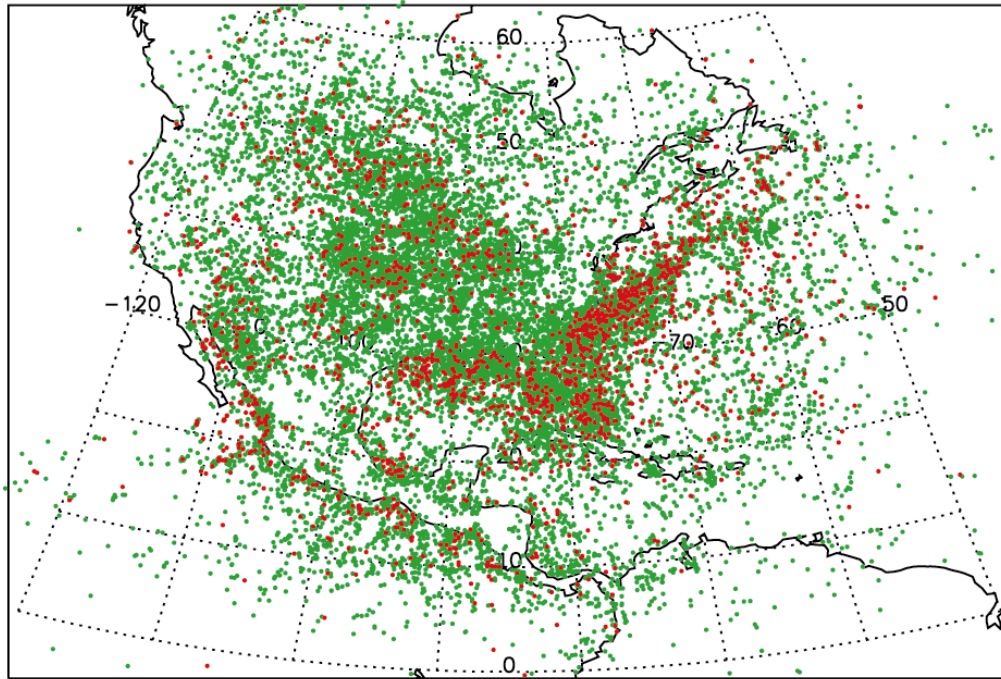


Figure 3

Figure 3. Geographic locations of FORTE/NLDN coincident events. Green dots for the overall events; red dots for the very narrow, return stroke-initiating events.

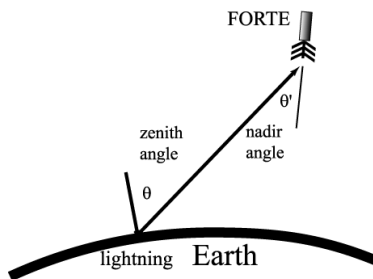


Figure 4

Figure 4. Geometry of the terrestrial lightning and the FORTE satellite.

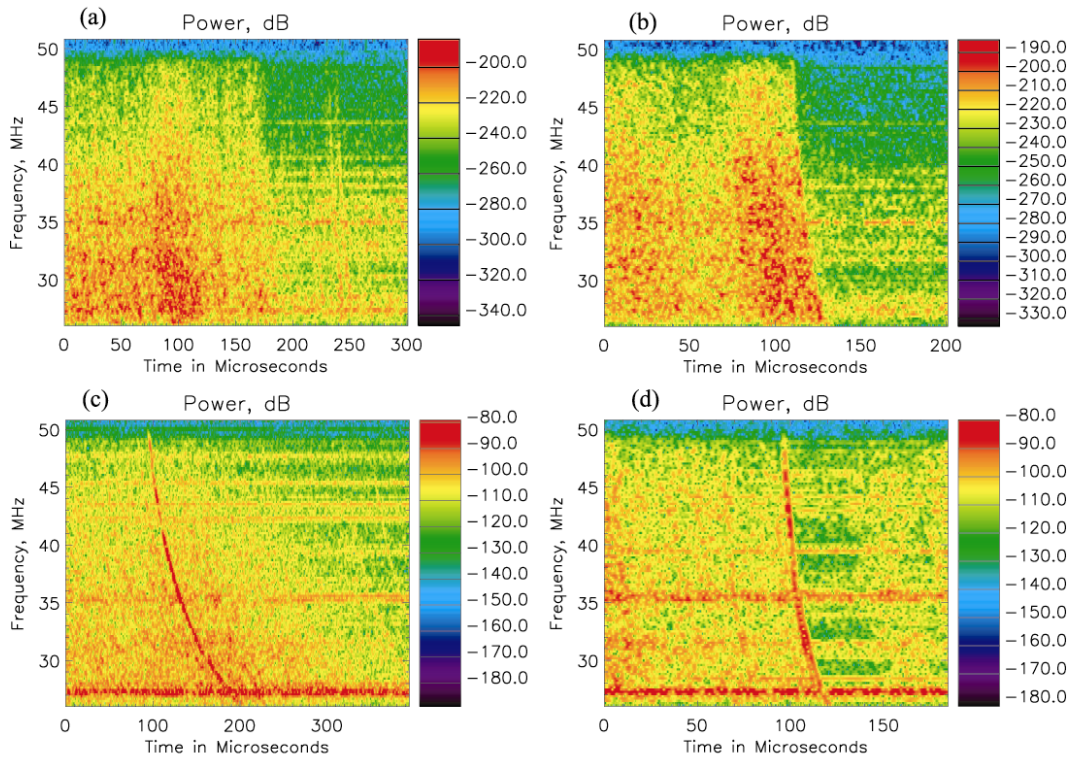


Figure 5

Figure 5. FORTE VHF observations of (a) a “normal” initial stroke, (b) a “normal” subsequent stroke, (c) an initial stroke started with a narrow pulse, and (d) a subsequent stroke started with a narrow pulse.

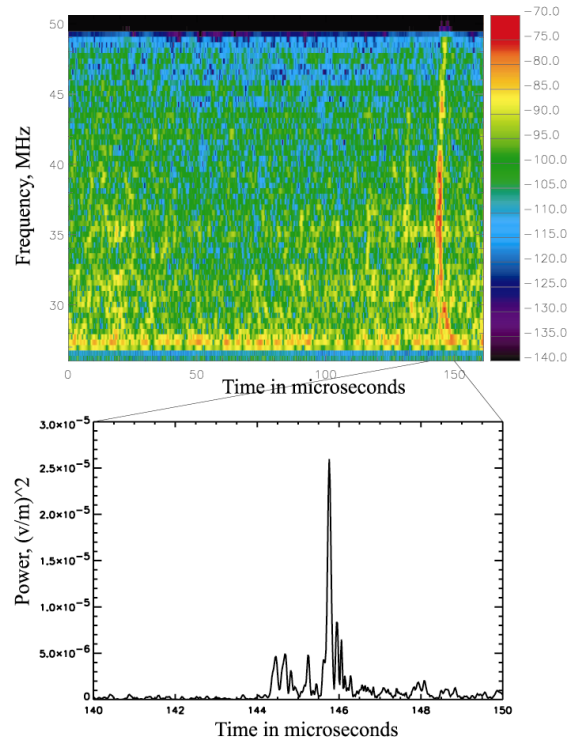


Figure 6

Figure 6. (a) Pulse in Figure 5c after the matched filtering deconvolution process. (b) Fine time waveforms of the radiation power around the pulse.

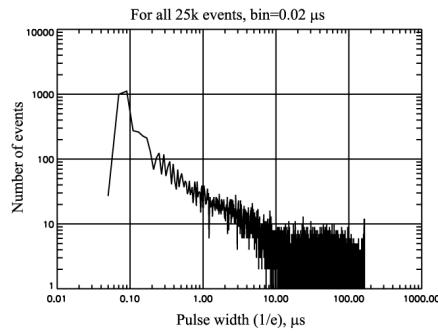


Figure 7

Figure 7. Pulse width ($1/e$ of peak power) distribution for all the coincident events. Pulses that are less than 100 ns wide are considered as narrow pulses in this study.

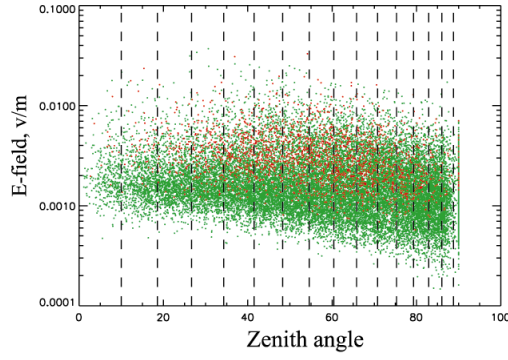


Figure 8

Figure 8. Peak radiation amplitudes (E) for all the parent events (green) and the narrow pulses (red), as functions of the zenith angle (Figure 4).

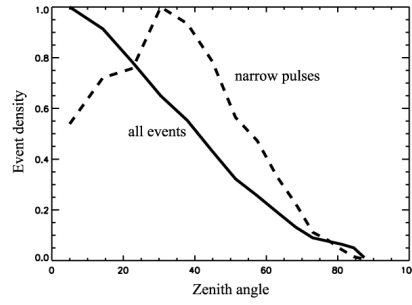


Figure 9

Figure 9. Distributions of earth area-normalized number of events (event density) at the angular bins shown in Figure 8. Solid curve is for the overall events and dashed curve is for the narrow pulses. Each curve is normalized to its maximum for the comparison.

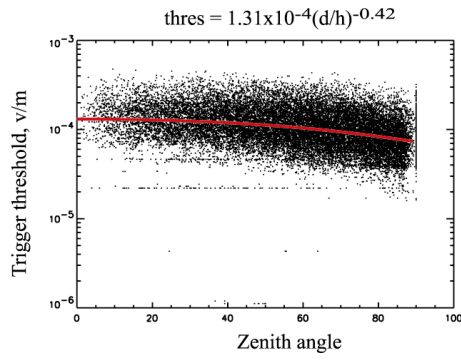


Figure 10

Figure 10. Apparent FORTE trigger thresholds for all the coincident events. Red line indicates the best power-law fit to the scattered points, $1.31 \times 10^{-4} (d/H)^{-0.42}$.

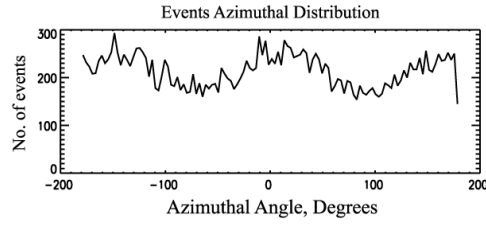


Figure 11

Figure 11. Event distribution around the azimuth angle as being viewed from the satellite. Slightly more events were triggered in the ram direction than in the cross-track direction due to the antenna directivity.

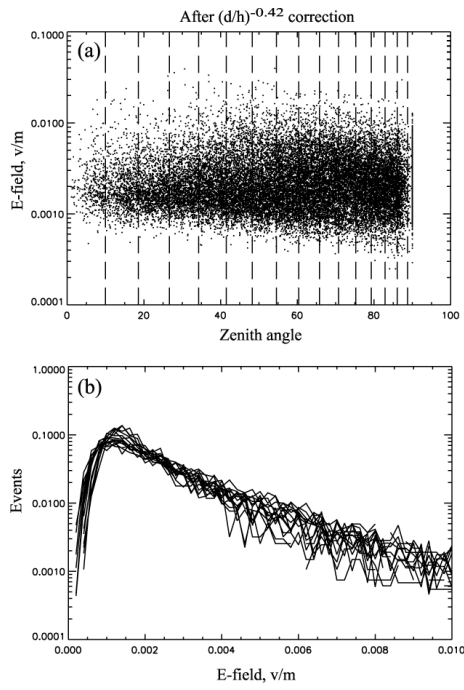


Figure 12

Figure 12. (a) “Threshold-corrected” peak E -fields for all the events. (b) E -field amplitude distributions at the 15 individual angular bins.

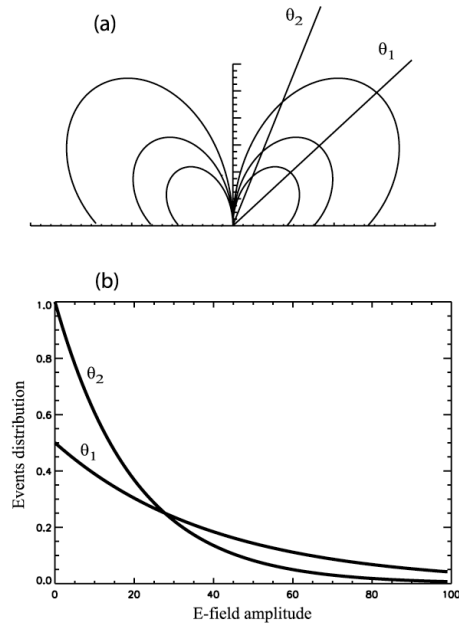


Figure 13

Figure 13. Relations between (a) the radiation beam pattern and (b) the angular-dependent amplitude distributions.

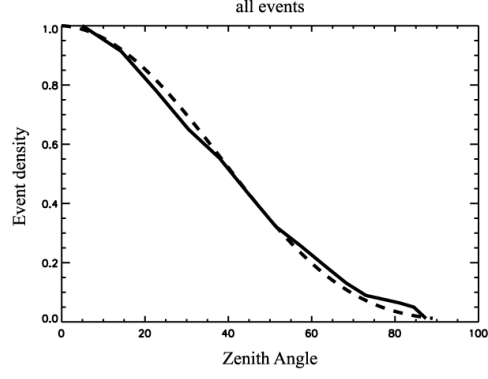


Figure 14

Figure 14. Comparing the event density distributions between the observed overall events (solid) and the model simulation (dashed, Equation 17). An isotropic model $b(\theta) = 1$ is used for the simulation.

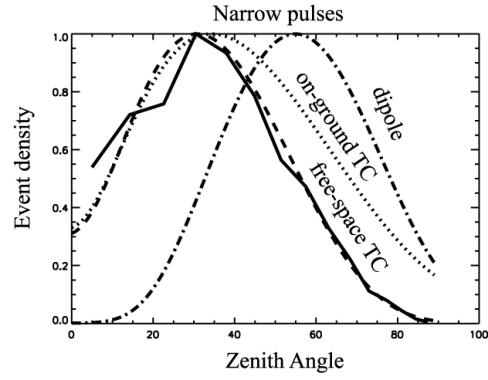


Figure 15

Figure 15. Comparing the event density distributions between the observed narrow pulses (solid) and the model simulations of a dipole (dot-dashed), an on-ground traveling current (dotted), and a free space traveling current (dashed). A statistic direction deviation of $\sigma(\theta) = 12^\circ$ from vertical ($\bar{\theta} = 0$) is used for the simulations. The speed v is assumed $0.75c$ for the two latter models.

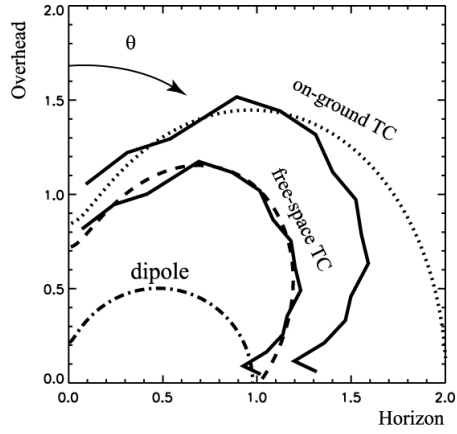


Figure 16

Figure 16. Direct beam pattern comparisons between that of the narrow pulses and the three different models. The former is inferred by comparing the event density distributions between the narrow pulses and the overall events, according to Equation 18. The models are the same as that presented in Figure 2.

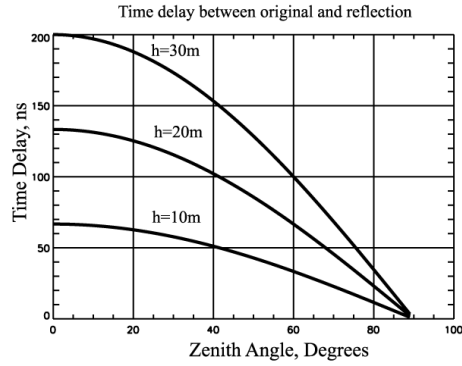


Figure 17

Figure 17. Time delays between the original and the reflected pulses at the satellite. For source 30 m above ground, the delay is greater than 50 ns at most of the zenith angles.

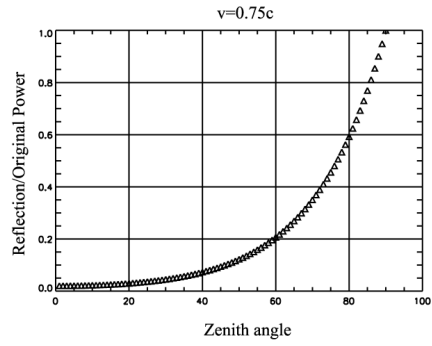


Figure 18

Figure 18. Power ratio of the reflected to the original pulse for $v = 0.75c$ free space traveling current radiation. At zenith angles less than 75° , the ratio is increasingly smaller than 0.5. Only near the horizon, powers from the two pulses are compatible.